Supplementary

Table S1 Basic patient information and pulmonary nodule characteristics

Variable	Index
Age	56.70±9.85
Sex	
Male/female	14/26
Body mass index	
<18.5 kg/m^2	5
18.5–24.9 kg/m^2	27
≥25 kg/m^2	8
Nodule type	
Solid/part-solid/ground-glass nodule	3/17/20
Complication	
None/hemorrhage/pneumothorax/hemorrhage + pneumothorax	11/14/10/5
Lobe	
RUL/RML/RLL/LUL/LLL	12/2/9/14/3
Pathology	
Malignant/benign	36/4
Surgical approach	
Minimally invasive surgery/thoracotomy	40/0
Wedge resection/segmentectomy/lobectomy/pneumonectomy	23/12/5/0

LLL, left lower lobe; LUL, left upper lobe; RLL, right lower lobe; RML, right middle lobe; RUL, right upper lobe.

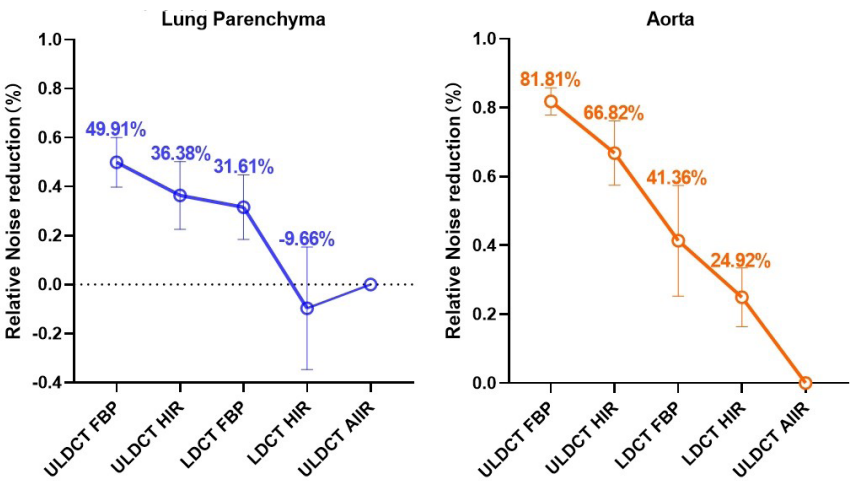

Figure S1 Relative reduction rate of noise in lung parenchyma and aorta. [Ratio = ($Noise_{other\ image}$-$Noise_{ULDCT\text{-}AIIR}$)/$Noise_{other\ image}$]. Solid circles represent mean values with error bars indicating standard deviations. LDCT, low-dose computed tomography; ULDCT, ultra-low-dose computed tomography; FBP, filtered-back projection; HIR, hybrid iterative reconstruction; AIIR, artificial intelligence iterative reconstruction.

https://dx.doi.org/10.21037/qims-2025-1544

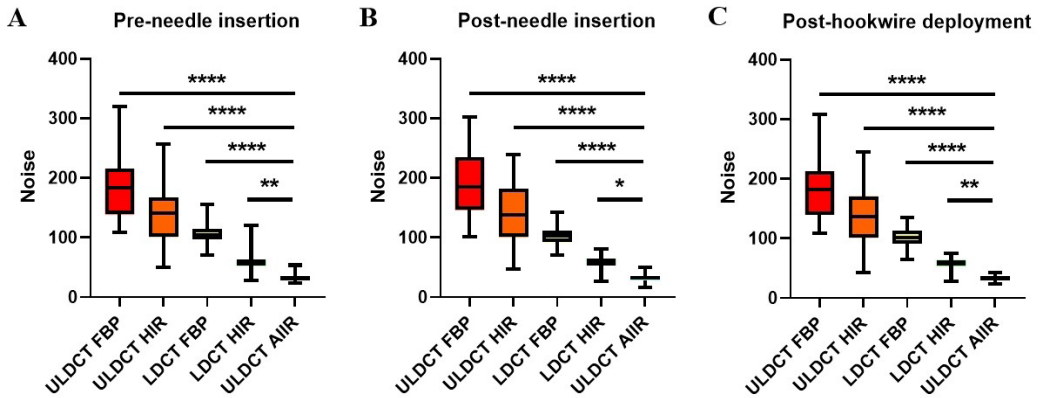

Figure S2 Aortic noise measured in each group's images during the puncture procedure. Box plots (A-C) display the aortic noise measured in images across experimental groups during the puncture procedure. The central line indicates the median, the box boundaries correspond to the first and third quartiles, and the whiskers represent the maximum and minimum values of the dataset respectively. ****, P<0.0001; **, P<0.01; *, P<0.05. AIIR, artificial intelligence iterative reconstruction; FBP, filtered-back projection; HIR, hybrid iterative reconstruction; LDCT, low-dose computed tomography; ULDCT, ultra-low-dose computed tomography.

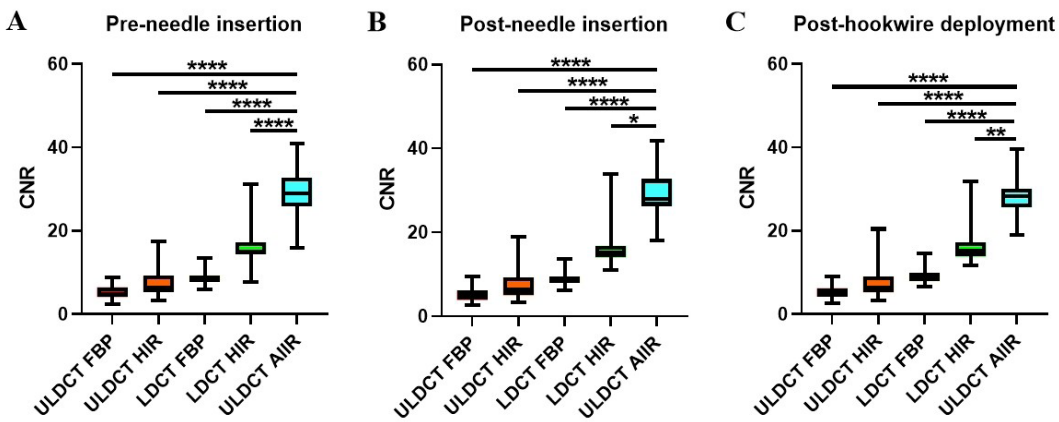

Figure S3 Aorta to lung contrast-to-noise ratio measured in each group's images during the puncture procedure. Box plots (A-C) display the lung parenchyma-to-aorta CNR measured in images across experimental groups. The central line indicates the median, the box boundaries correspond to the first and third quartiles, and the whiskers represent the maximum and minimum values of the dataset respectively. ****, P<0.0001; **, P<0.01; *, P<0.05. AIIR, artificial intelligence iterative reconstruction; CNR, contrast-to-noise ratio; FBP, filtered-back projection; HIR, hybrid iterative reconstruction; LDCT, low-dose computed tomography; ULDCT, ultra-low-dose computed tomography.

https://dx.doi.org/10.21037/qims-2025-1544

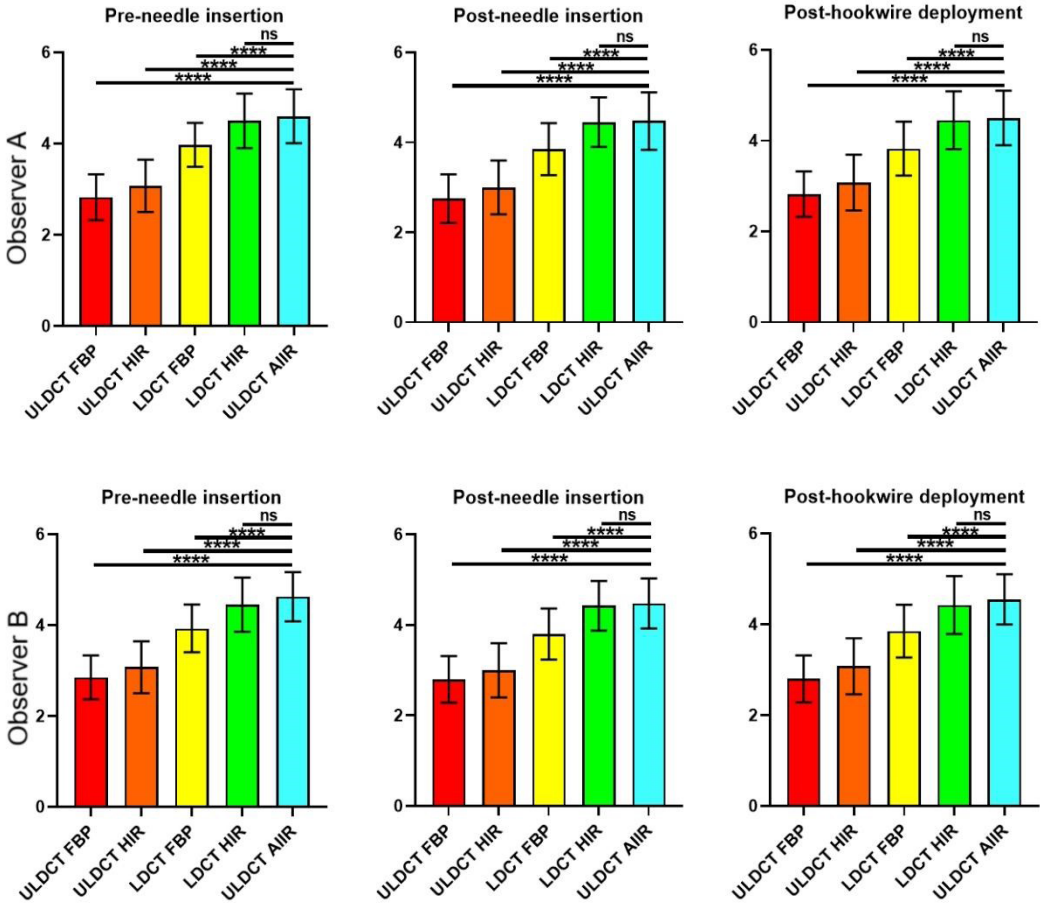

Figure S4 Subjective scoring of pulmonary nodule clarity by two observers. ****, P<0.0001; ns, non-significant. AIIR, artificial intelligence iterative reconstruction; FBP, filtered-back projection; HIR, hybrid iterative reconstruction; LDCT, low-dose computed tomography; ULDCT, ultra-low-dose computed tomography.

https://dx.doi.org/10.21037/qims-2025-1544

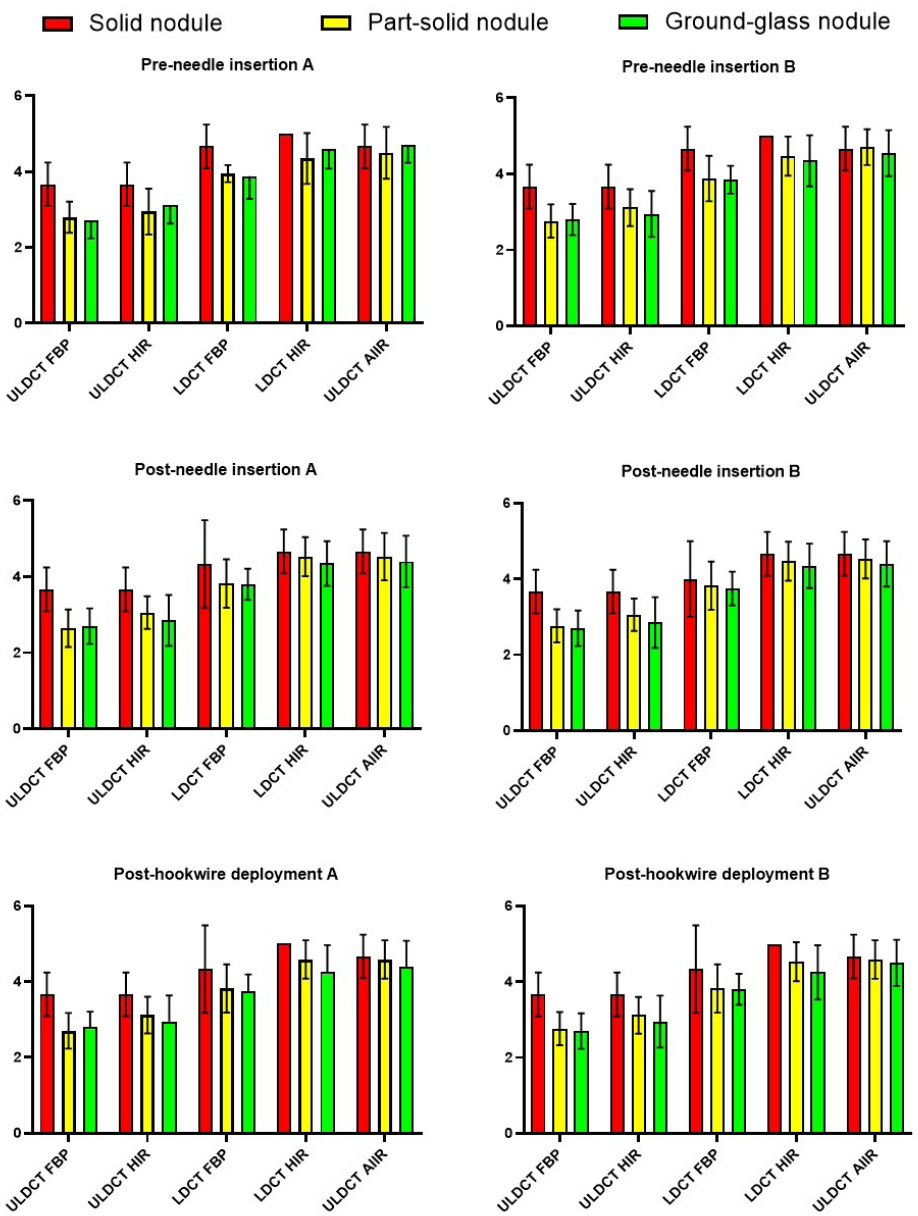

Figure S5 Subjective scoring of nodule clarity across different attenuation levels by two observers [A,B]. AIIR, artificial intelligence iterative reconstruction; FBP, filtered-back projection; HIR, hybrid iterative reconstruction; LDCT, low-dose computed tomography; ULDCT, ultra-low-dose computed tomography.

https://dx.doi.org/10.21037/qims-2025-1544

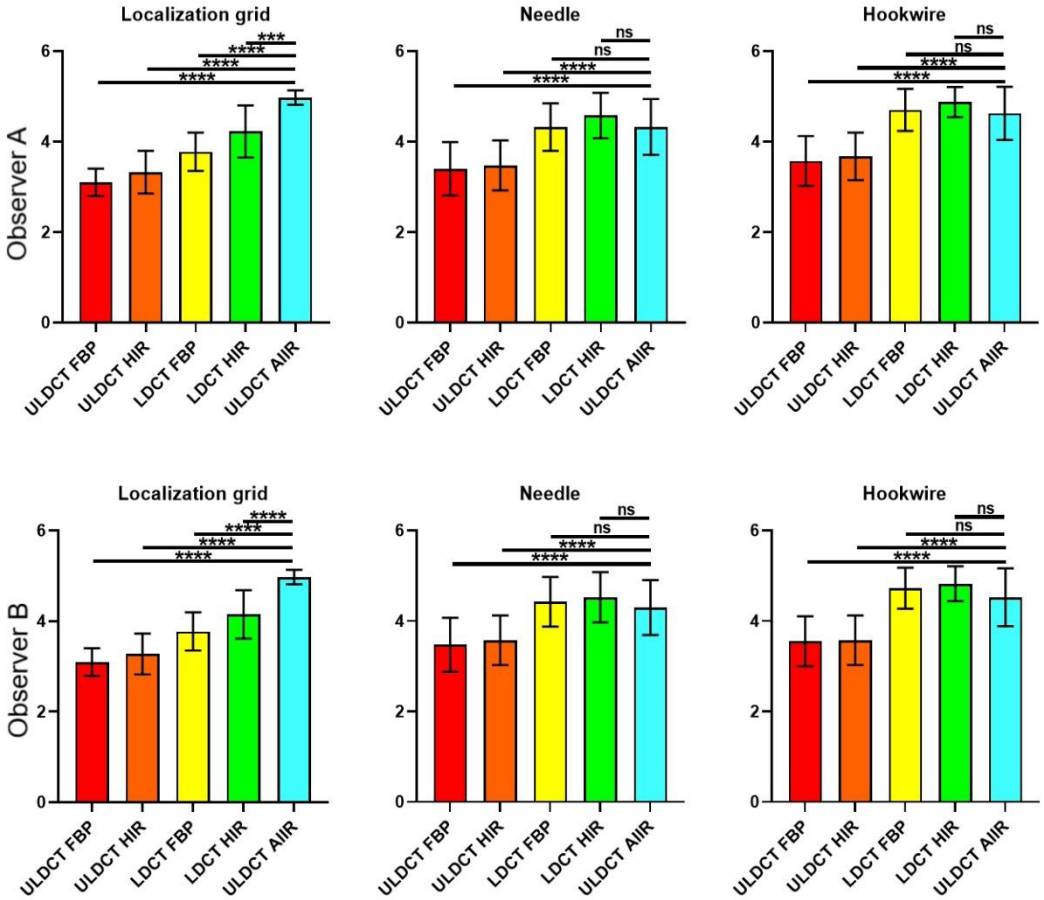

Figure S6 Subjective scoring of localization grid, needle, and hook-wire clarity by two observers. ****, P<0.0001; ***, P<0.001; ns, non-significant. AIIR, artificial intelligence iterative reconstruction; FBP, filtered-back projection; HIR, hybrid iterative reconstruction; LDCT, low-dose computed tomography; ULDCT, ultra-low-dose computed tomography.

https://dx.doi.org/10.21037/qims-2025-1544

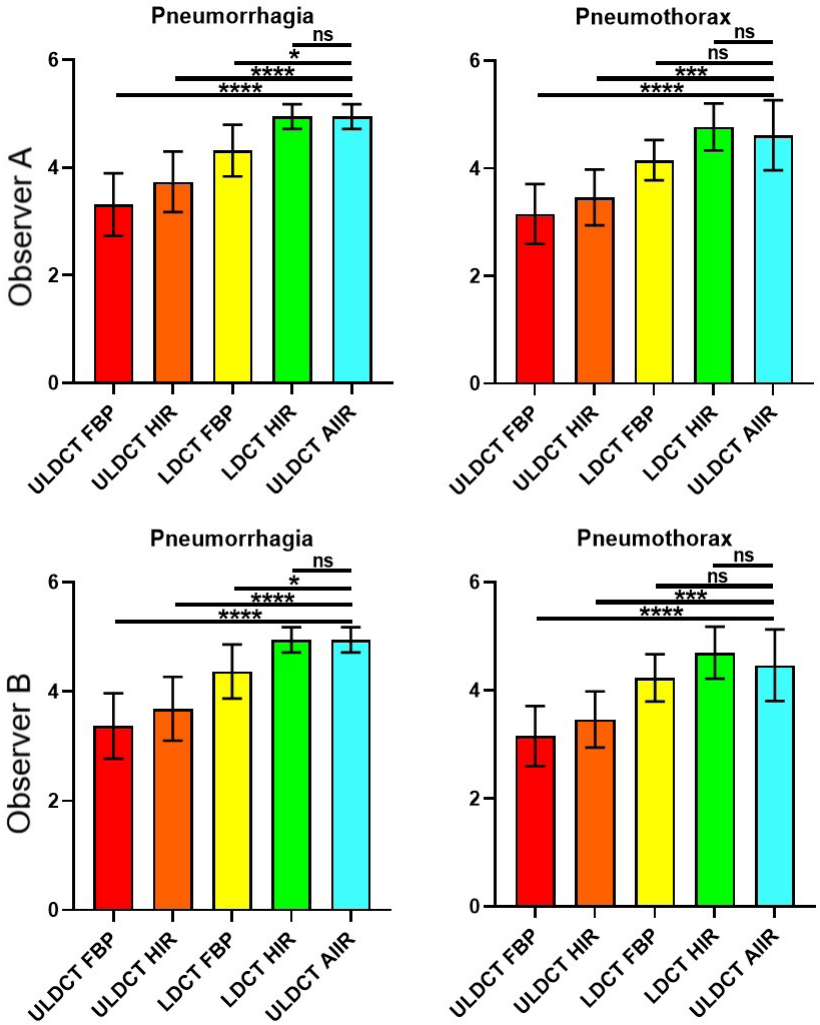

Figure S7 coring of clarity for post-puncture pulmonary hemorrhage and pneumothorax by two observers. ****, P<0.0001; ***, P<0.001; *, P<0.05; ns, non-significant. AIIR, artificial intelligence iterative reconstruction; FBP, filtered-back projection; HIR, hybrid iterative reconstruction; LDCT, low-dose computed tomography; ULDCT, ultra-low-dose computed tomography.

https://dx.doi.org/10.21037/qims-2025-1544